



# Superinsulating nanocellulose aerogels: Effect of density and nanofiber alignment

Deeptanshu Sivaraman<sup>a,b,\*</sup>, Gilberto Siqueira<sup>c</sup>, Anjani K. Maurya<sup>d</sup>, Shanyu Zhao<sup>a</sup>, Matthias M. Koebel<sup>a</sup>, Gustav Nyström<sup>c,e</sup>, Marco Lattuada<sup>b</sup>, Wim J. Malfait<sup>a</sup>

<sup>a</sup> Empa – Building Energy Materials and Components, Swiss Federal Laboratories for Materials Science and Technology, Dübendorf, Switzerland

<sup>b</sup> Department of Chemistry, University of Fribourg, Fribourg, Switzerland

<sup>c</sup> Cellulose & Wood Materials Laboratory, Empa – Swiss Federal Laboratories for Materials Science and Technology, Dübendorf, Switzerland

<sup>d</sup> Empa – Center for X-ray Analytics, Swiss Federal Laboratories for Materials Science and Technology, Empa, St. Gallen, Switzerland

<sup>e</sup> Department of Health Sciences and Technology, ETH Zürich, 8092 Zürich, Switzerland

## ARTICLE INFO

### Keywords:

Cellulose nanofibers  
CNF  
Aerogel  
Thermal conductivity  
SAXS  
E modulus

## ABSTRACT

Cellulose aerogels are potential alternatives to silica aerogels with advantages in cost, sustainability and mechanical properties. However, the density dependence of thermal conductivity ( $\lambda$ ) for cellulose aerogels remains controversial. Cellulose aerogels were produced by gas-phase pH induced gelation of TEMPO-oxidized cellulose nanofibers (CNF) and supercritical drying. Their properties are evaluated by varying the CNF concentration (5–33 mg·cm<sup>-3</sup>) and by uniaxial compression (9–115 mg·cm<sup>-3</sup>). The aerogels are transparent with specific surface areas of ~400 m<sup>2</sup>·g<sup>-1</sup>, mesopore volumes of ~2 cm<sup>3</sup>·g<sup>-1</sup> and a power-law dependence of the E-modulus ( $\alpha \sim 1.53$ , and the highest reported E of ~1 MPa). The dataset confirms that  $\lambda$  displays a traditional U-shaped density dependence with a minimum of 18 mW·m<sup>-1</sup>·K<sup>-1</sup> at 0.065 g·cm<sup>-3</sup>. For a given density,  $\lambda$  is ~5 mW·m<sup>-1</sup>·K<sup>-1</sup> lower for compressed aerogels due to the alignment of nanofibers, confirmed by small angle X-ray scattering (SAXS).

## 1. Introduction

Cellulose is a naturally occurring semi-crystalline biopolymer, and the most abundant biopolymer on Earth (Mathew et al., 2006). It is the structural component of cell walls of plants and wood, but is also produced by bacteria, amoeba and algae. The majority of commercially available cellulose is refined from wood. Their differing origins impart them with varying structures and properties (Heinze et al., 2018) including depending on the contents of lignin and hemicellulose (Hon, 1995). Cellulose consists of C6-rings of  $\beta$ -(1-4)-D-Glucopyranose, that form straight chains or branched chains, with plenty of accessible hydroxyl groups which give rise to further functionalities (Kamide, 2005). Over the last decade, there has been a rapid increase in cellulose research for applications in the food and packaging industry (Rhim & Ng, 2007), biocatalysis (Abdul Khalil et al., 2020), the building and construction sector (Plappert, Quraishi, Nedelec, Konnerth, Rennhofer, Lichtenegger, and Liebner, 2018a), bio-medical and pharmaceutical fields (Dri et al., 2014), energy storage (Aeby et al., 2021), and textiles

(Maciel et al., 2019).

Cellulose is extracted from its constituents by mechanical and/or chemical processes, which give a fibrillar network structure in the micro- or nanoscale (defined by their diameter) depending on the fibrillation conditions (Chu et al., 2020). Cellulose has a variable degree of crystallinity, depending on fiber length and the nanocellulose preparation conditions, where typically the shorter and rigid cellulose nanocrystals (CNC) contain mainly crystalline cellulose and the longer cellulose nanofibers (CNF) containing both crystalline and amorphous fragments (Nascimento et al., 2015). CNFs are produced by disintegration of plant based sources (Johansson et al., 2011) and one common route is to use TEMPO (2,2,6,6-tetramethylpiperidine-1-oxyl) mediated oxidation along with a mechanical disintegration process, which both reduces the energy consumption and results in nanofibers with higher chemical reactivity and negative surface charge (Isogai et al., 2011). These nanofibers display higher specific surface areas, higher aspect ratios and better mechanical properties (Sun et al., 2021) and are particularly suited toward porous material applications such as

\* Corresponding author at: Empa – Building Energy Materials and Components, Swiss Federal Laboratories for Materials Science and Technology, Dübendorf, Switzerland.

E-mail address: [deeptanshu.sivaraman@empa.ch](mailto:deeptanshu.sivaraman@empa.ch) (D. Sivaraman).

<https://doi.org/10.1016/j.carbpol.2022.119675>

Received 1 March 2022; Received in revised form 9 May 2022; Accepted 27 May 2022

Available online 3 June 2022

0144-8617/© 2022 The Authors. Published by Elsevier Ltd. This is an open access article under the CC BY license (<http://creativecommons.org/licenses/by/4.0/>).

substrates for catalysis (Vareda et al., 2016), nanotechnology (Qian et al., 2019), pharmacology (García-González et al., 2019) and thermal insulation (Ahankari et al., 2021; Dri et al., 2014; Plappert et al., 2017).

Aerogels are nanomaterials with remarkable properties, including ultra-low density ( $0.002\text{--}0.5\text{ g}\cdot\text{cm}^{-3}$ ) and high surface area ( $100\text{--}2000\text{ m}^2\cdot\text{g}^{-1}$ ) (Aegerter et al., 2011; Hüsing & Schubert, 1998). Early biopolymer aerogels were made using gelatin (Kistler, 1931), starch (Baudron et al., 2019), pectin (Rudaz et al., 2014), chitosan (Guerrero-Alburquerque et al., 2020) and alginate (Raman et al., 2015), but cellulose has become the dominant biopolymer for aerogel research (Apostolopoulou-Kalkavoura et al., 2020) and accounts for 80 % of recent publications (Zhao et al., 2018). Vacuum and ambient pressure dried mesoporous cellulose aerogels (or 'xerogels') fail to preserve the porosity of the matrix due to the capillary forces and pore collapse during drying, unless specific precautions are taken (Yamato et al., 2021; Zhao et al., 2015). Freeze drying is the most widely used procedure for cellulose aerogel synthesis, but the resulting materials generally lack the mesoporosity and ultra-low thermal conductivity typical for aerogels because of the large secondary pores due to ice crystal growth (Zou & Budtova, 2021). Although directionally freeze dried structures can have moderately low  $\lambda$  values (Berglund et al., 2021), supercritical drying (SCD) remains necessary to preserve the mesoporosity and produce superinsulating materials (Gavillon & Budtova, 2008; Hoepfner et al., 2008; Innerlohinger et al., 2006; Jin et al., 2004; Kobayashi et al., 2014; Liebner et al., 2008; Plappert et al., 2017).

Commodity building insulation materials such as mineral wool display a U-shaped correlation between  $\lambda$  and density with a minimum  $\lambda$  of  $30\text{--}40\text{ mW}\cdot\text{m}^{-1}\cdot\text{K}^{-1}$  (Aegerter et al., 2011; Alam et al., 2011; Koebel et al., 2012). Here, the initial decrease in  $\lambda$  with increasing density results from the suppression of gas convection and radiative contributions as the pores decrease in size. In aerogels, the gas phase conduction component can be partially suppressed, through the Knudsen effect, leading to  $\lambda$  values lower than that of standing air ( $26\text{ mW}\cdot\text{m}^{-1}\cdot\text{K}^{-1}$  at STP). Silica aerogels display a U-shaped density dependence of  $\lambda$ , with a minimum of  $<15\text{ mW}\cdot\text{m}^{-1}\cdot\text{K}^{-1}$  at  $100\text{--}150\text{ mg}\cdot\text{cm}^{-3}$  (Fricke et al., 1992; Iswar et al., 2021; Wong et al., 2014). Other aerogel systems display a similar density dependence of  $\lambda$  with minima in  $\lambda$  at comparable densities, e.g. resorcinol-formaldehyde at  $\sim 160\text{ mg}\cdot\text{cm}^{-3}$  (Fricke et al., 1992), polyurea-polyurethane at  $\sim 220\text{ mg}\cdot\text{cm}^{-3}$  (Lee et al., 2009; Zhu et al., 2017) and hybrid organic-inorganic systems at  $\sim 100\text{--}250\text{ mg}\cdot\text{cm}^{-3}$  (Lu, Arduini-Schuster, Kuhn, Nilsson, Fricke, and Pekala, 1992a; Lu, Wang, Arduini-Schuster, Kuhn, Büttner, Nilsson, Heinemann, and Fricke, 1992b). For cellulose however, we see controversial results, with the optimum density to minimize  $\lambda$ : whereas Kobayashi (Kobayashi et al., 2014) observed a  $\lambda$  of  $18\text{ mW}\cdot\text{m}^{-1}\cdot\text{K}^{-1}$  at  $17\text{ mg}\cdot\text{cm}^{-3}$ , Plappert (Plappert et al., 2017) found a minimum of  $17\text{ mW}\cdot\text{m}^{-1}\cdot\text{K}^{-1}$  at  $87\text{ mg}\cdot\text{cm}^{-3}$ . The latter observation is more in line with other aerogel materials and more consistent with our understanding of how pore size and the Knudsen effect influence thermal conductivity in aerogels (Zhao et al., 2018, 2020).

In this study, we investigate the effect on important aerogel properties (mechanical,  $\lambda$ , fiber alignment) over a wide range of densities ( $5\text{--}115\text{ mg}\cdot\text{cm}^{-3}$ ) of TEMPO-CNF aerogels to solve the debate of  $\lambda$  as a function of density. We intend to investigate the effects of fiber and pore alignment, which are in turn responsible for heat flow in CNF aerogels.

## 2. Materials and methods

### 2.1. Materials

Never-dried elemental chlorine free (ECF) cellulose fibers from bleached softwood pulp (*Picea abies* and *Pinus* spp.) were acquired from Stendal GmbH (Berlin, Germany). 2,2,6,6-Tetramethyl-1-piperidinyloxy (TEMPO) and sodium hypochlorite (NaClO) solution (12–14 % chlorine) were procured from VWR international. Sodium bromide (NaBr  $\geq 99\%$ ) and sodium hydroxide (NaOH  $\geq 99\%$ ) were supplied by

Carl Roth GmbH. Hydrochloric acid (HCl; 35.5–38 % v/v in water) was sourced from abcr swiss AG, and denatured ethanol (95 % ethanol/5 % 1-propanol v/v. %) was sourced from Alcosuisse AG.

### 2.2. Aerogel synthesis

TEMPO-mediated cellulose fiber oxidation is performed as per previously published protocols and is mentioned in detail in the supplementary information (Isogai et al., 2011; Weishaupt et al., 2015; Wu et al., 2020). Briefly, the oxidized cellulose fibers are processed in a Supermass Colloider (MKZA10-20J CE Masuko Sangyo, Japan) at an applied energy of 9 kWh (Fig. 1a). The CNF concentration after this step was 1.3 wt% in water. The suspension was subsequently diluted to 0.5 wt% and further mechanically fibrillated using a high shear homogenization process (M110EF, Microfluidics Ind., Newton, MA-USA). After homogenization, the remaining agglomerates were removed with a Branson Digital horn sonifier.

To produce the hydrogels, 40 mL of the CNF suspension was transferred in a mold ( $53 \times 53 \times 30\text{ mm}$ ), which was placed inside a container (Fig. 1b). Gelation was carried out by an acidic-vapor phase pH change method (Wu et al., 2020): about 1 mL of 37 % HCl was placed inside the closed container, next to the mold with the suspension. The suspension was kept inside the acidic atmosphere at room temperature for 2 h. The syneresis fluid ( $\sim 1\text{ mL}$ ) was discarded and a solid transparent hydrogel was obtained. The hydrogels were solvent exchanged in stages (30, 75, 90 %) to 99 % ethanol, and dried in a continuous supercritical extraction process (Separex, France) in a 500 mL autoclave, for 6 h at  $50^\circ\text{C}$ , 120 bar and with a  $\text{CO}_2$  circulation of  $20\text{ g}/\text{min}$ .

Aerogels with variable density were prepared in two different ways. Suspensions with a higher CNF concentration were prepared through vacuum distillation (Rotavap, BÜCHI Labortechnik AG, Switzerland) at  $50^\circ\text{C}$ , 65 mbar for variable durations (1–4 h) depending on the targeted final concentration. This process is limited to at most 3.0 wt% CNF, corresponding to a final aerogel density of  $33\text{ mg}\cdot\text{cm}^{-3}$ , by the rapidly increasing suspension viscosity. The second approach to prepare higher density CNF aerogels relies on irreversible densification. Cuboidal samples ( $45 \times 45 \times 10\text{ mm}^3$ ) were compressed to different final strain values (20–95 %) to aerogel density range up to  $115\text{ mg}\cdot\text{cm}^{-3}$ .

### 2.3. Characterization

#### 2.3.1. Density

All samples analyzed were monolithic and regular in shape, therefore a weighing scale and calipers were used to measure envelope density. The skeletal density of cellulose aerogels was taken to be  $1.6\text{ g}\cdot\text{cm}^{-3}$  (Rudaz et al., 2014).

#### 2.3.2. $\text{N}_2$ sorption analysis

The surface area was determined by nitrogen sorption measurements on a Micromeritics 3flex device, where weighed samples ( $\sim 25\text{--}30\text{ mg}$ ) were degassed to 0.016 mbar at  $75^\circ\text{C}$  for 18 h prior to analysis. The sorption isotherms were acquired for 50 pressure points in the 0.001–0.998 P/P<sub>0</sub> range, with an equilibration time of 10 s per incremental  $\text{N}_2$  addition and 600 s per pressure condition. The specific surface area was derived using the BET model ( $S_{\text{BET}}$ ;  $\text{m}^2\cdot\text{g}^{-1}$ ) and the specific pore volume using the BJH model ( $V_{\text{BJH}}$ ;  $\text{cm}^3\cdot\text{g}^{-1}$ ).  $V_{\text{pore}}$  and  $D_{\text{pore}}$  were also calculated from the envelope and skeletal density and surface area. The calculation of  $D_{\text{pore}}$  is undoubtedly complex and the definition of a pore 'size' is non-trivial. We choose a hexagonal pore arrangement as hydrocarbon fibrous materials orient themselves in maximal surface to volume polygons, e.g. natural fiber schemas and freeze-dried aerogels. We acknowledge the lack of an actual hexagonal arrangement, but it may be a better approximation than cylindrical pores (Z. Wang, 2019; Zhang et al., 2015).

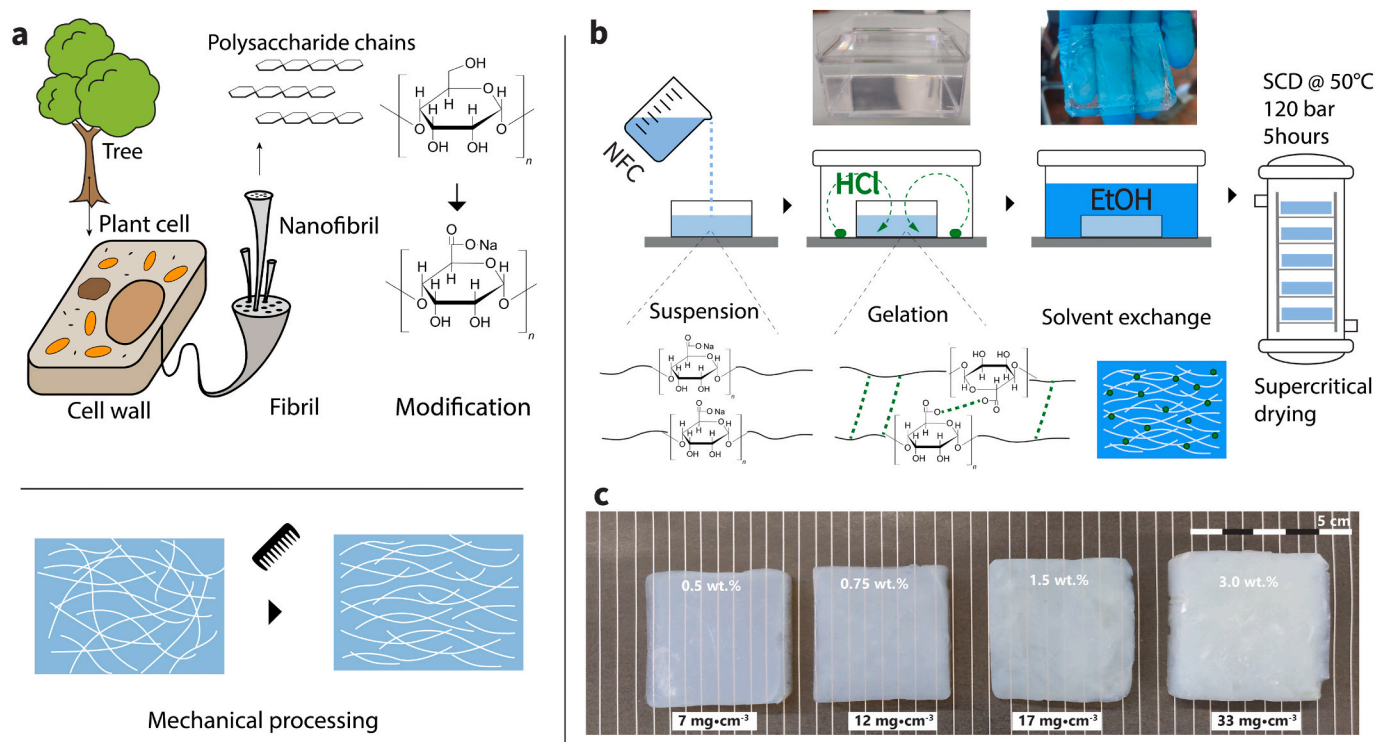


**Fig. 1.** a) TEMPO-NFC production process involving chemically-assisted mechanical nanofibrillation b) gas-phase gelation methodology for producing transparent monolithic CNF aerogels, c) aerogels of different densities produced by concentration of the CNF suspension.

$$V_{\text{pore}} = \frac{1}{\rho_{\text{envelope}}} - \frac{1}{\rho_{\text{skeletal}}} \quad (1)$$

$$D_{\text{pore}} = \frac{4 \cdot V_{\text{pore}}}{\sqrt{3} \cdot S_{\text{BET}}} \quad (2)$$

### 2.3.3. SEM

Scanning electron microscopy (SEM) images were obtained using a FEI Nova NanoSEM 230 instrument (FEI, Hillsboro, Oregon, USA) at an accelerating voltage of 5 kV, a spot size of 2.0 and a working distance of 4 mm. One should note that, these aerogels easily damage under the electron beam and several stabilizing tweaks are needed. A platinum coating of 10 nm was applied to avoid charging during imaging. They were compiled using ImageJ.

### 2.3.4. Mechanical compression

Uniaxial compression tests were performed on cylindrical samples of aspect ratio 2:1 (height to diameter), made plane parallel by cutting the alcogels (before drying) using a universal materials testing machine (Zwick/Z010, Zwick/Roell, Germany) equipped with a 2 kN force transducer cell (KAP-S, AST Gruppe GmbH, Germany) in a controlled environment (temperature = 23 °C; relative humidity = 50 ± 5 %). The compression rate was kept at 1 mm/min until a pre-defined strain value was reached. The elastic moduli were calculated from the slope of the initial linear phase (3–5 % strain) of the curve.

### 2.3.5. Thermal conductivity

$\lambda$  was measured with a custom-built, miniaturized guarded two-plate device (shielded in the XY plane), calibrated from industry standard measurements for an expanded polystyrene and other aerogel samples of 500 × 500 mm<sup>2</sup>, according to ISO 12667/European Standard EN12667:2001 (Stahl et al., 2012) within the range of 5–100 mW·m<sup>-1</sup>·K<sup>-1</sup>. 45 × 45 × 10 mm<sup>3</sup> CNF aerogel samples were equilibrated in the atmosphere of room where the device was located (23 °C, ~40 % humidity) for 24 h before measurements. The temperature of the

cold plate was around 20 °C (uncontrolled) and the hot plate was maintained at 30 °C. Each sample was measured for 1 h and the steady-state heat flow was measured to calculate  $\lambda$ , after calibration and correction factors (Hammerschmidt, 2002). The thickness of the compressed samples was outside that of the calibration range and therefore they were stacked and measured together. Note that air layers between the stacked samples would increase the measured  $\lambda$  because the  $\lambda$  of standing air is higher than that of the compressed samples, and hence the actual  $\lambda$  would be lower than the reported values. However, the compressed samples were very smooth and plane-parallel, which allows for a clean stacking (Fig. 2f) and prevents air between the stacked samples, and effects on  $\lambda$  are expected to be below 0.5 mW·m<sup>-1</sup>·K<sup>-1</sup>. Note that the  $\lambda$  measurements were conducted in the direction of compression, because of strong fiber and pore nematic alignment,  $\lambda$  is expected to be (strongly) anisotropic in these samples. However, accurate  $\lambda$  measurements perpendicular to the compression direction are not possible due to size (and device) constraints and are not reported.

### 2.3.6. Small angle X-ray scattering (SAXS)

Samples after uniaxial compression to different strains (0–95 %) were oriented parallel to compression and heat flow direction (XY), and the beam perpendicular to compression and heat flow direction (XZ) (similar for heat flow direction, Fig. S3). Background measurements were carried out without sample in the beam. SAXS profiles were recorded with a Nanostar instrument (Bruker AXS GmbH, Karlsruhe, Germany) equipped with a micro-focused X-ray source (Incoatec GmbH, Geesthacht, Germany), with a beam spot size of about 400 μm, Cu-K $\alpha$  radiation ( $\lambda$  = 0.154 nm). A VANTEC-2000 Xe-based gas avalanche detector placed 5 cm (Wide angle X-ray scatter), 27 cm (difference in scatter pattern), and 107 cm (Small-angle X-ray scatter) from the sample. The detector has dimensions of 2048 × 2048 pixels, each 68 × 68 μm<sup>2</sup> size, and a photon-counting rate of 0.5 s<sup>-1</sup>. The minimum reliable scattering vector magnitude,  $q_{\text{min}}$ , is ~0.07 nm<sup>-1</sup>, with  $q = (4\pi/\lambda)\sin\theta$ , where  $2\theta$  is the scattering angle. The measurements were carried out under vacuum (~0.01 mbar) to minimize the air scattering. All samples



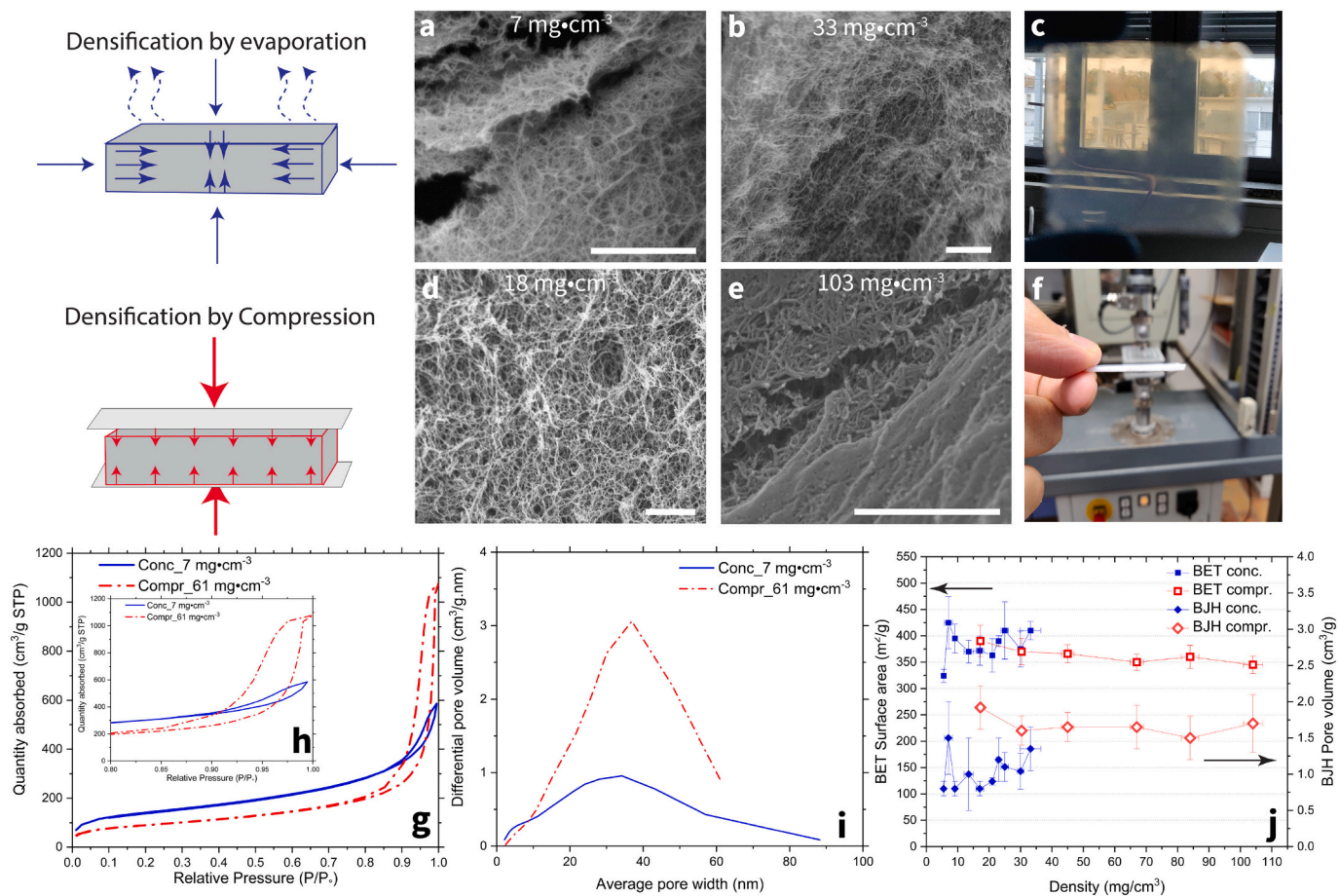


**Fig. 2.** a, b) SEM images of samples produced through concentration via vacuum distillation; c) concentrated CNF aerogel (12 mg·cm<sup>-3</sup>); d, e) SEM images of samples produced through post-drying mechanical compression. Scale bar is 1 μm in all images. f) Compressed CNF sample (85 mg·cm<sup>-3</sup>). g) nitrogen sorption isotherms (full range in P/P<sub>0</sub>), h) sorption isotherms, P/P<sub>0</sub> 0.8–1.0, i) pore size distribution, j) BET surface area and BJH pore volume as a function of density.

were measured for 60 s and placed at an angle of around 45° to ensure the beam-stop holder wires did not interfere with the scattering at 0–90°. The special and flood fields corrected scattering profiles were processed using a python script for reduction and analysis, using open source modules for SAXS data Fabio and pyFAI (Kieffer & Wright, 2013; Knudsen et al., 2013). Integration was carried out along azimuthal angle and radial directions, with corrections for the beam center, with scatter patterns being rotated by 45° to account for initial sample placement. Final data was analyzed and plotted using matplotlib, plotly and lmfit (Newville et al., 2014) (scripts available). Fiber orientation is calculated based on the Degree of Preferred Orientation (DPO), Herman's order parameter,  $f$  and the Ruland's misorientation width (defined in supplementary text) (Fourmann et al., 2021; Maurya et al., 2021; Putz et al., 2017; Saxe et al., 2014; Siqueira et al., 2017). To extract the Ruland's width ( $B_\phi$ ), the radial integration profile is normalized to a sum of two Lorentzian functions (Maurya et al., 2021; Ran et al., 2001).

$$DPO = \frac{\text{Area under peaks, } I(\phi)}{\text{Total area under curve}} \quad (3)$$

$$\langle \cos^2 \phi \rangle_{hkl} = \frac{\int_0^\pi I(\phi) \cos^2 \phi \sin \phi \, d\phi}{\int_0^\pi I(\phi) \sin \phi \, d\phi} \quad (4)$$

$$\langle \cos^2 \gamma \rangle = 1 - 2 \langle \cos^2 \phi \rangle \quad (5)$$

$$f \text{ (Herman's parameter)} = \frac{3 \langle \cos^2 \gamma \rangle - 1}{2} \quad (6)$$

$$B_{obs} = \frac{1}{L_f^* q} + B_\phi \quad (7)$$

### 3. Results

#### 3.1. Cellulose aerogels

Nanocellulose hydrogels have been prepared by a novel gas-phase route which leads to physical gelation due to increased hydrogen bonding and stable hydrogel structure formation by fiber linking (Fig. 1a). This physical gelation process is not completely reversible by increasing pH, but the large monolith reduces to smaller agglomerates (Nordenström et al., 2017). The cellulose aerogels display the typical 'blue' hue associated with mesoporous networks (Fig. 1c). Low CNF concentration aerogels have a high optical transparency, up to 80 % transmittance at 600 nm for a 10 mm thick sample, decreases with increasing CNF concentration due to change in pore size and heterogeneity (Fig. S1). As expected, the aerogel density correlates with CNF concentration (Fig. 1c, Table S1). The low CNF concentration aerogels show higher shrinkage (<1 wt%; shrinkage around 10 %) than higher concentration aerogels due to the higher fiber density provides increased structural rigidity, consistent with literature for biopolymer aerogels (Gurikov et al., 2019; Mandal et al., 2019).

#### 3.2. Pore morphology and structure

The morphologies of cellulose aerogels with different densities



produced by suspension concentration ( $7\text{--}33\text{ mg}\cdot\text{cm}^{-3}$ ) and by irreversible compression ( $9\text{--}103\text{ mg}\cdot\text{cm}^{-3}$ ) are compared in Fig. 2. All samples consist of an intertwined fiber network typical for CNF aerogels (Groult & Budtova, 2018; Plappert et al., 2017) and chitosan aerogels (Takeshita et al., 2020). The average fiber diameter, estimated from SEM through image analysis, was  $15 \pm 3.5\text{ nm}$ , which is considerably higher than the  $2\text{--}4\text{ nm}$  fiber diameter estimated by AFM for the starting CNF suspension (Fig. S2), or the  $4\text{--}5\text{ nm}$  expected from the literature for TEMPO-CNF (Arcari et al., 2019; Seantier et al., 2016). The higher density aerogel prepared by suspension concentration (Fig. 2b) has a similar network structure to the lower density aerogels (Fig. 2a), without any ordering into sheets or perceivable preferred orientation, but rather a systemic entanglement of fibers.

The surface area scatters significantly, but independent of aerogel density for the aerogels prepared by concentration (Fig. 2j, Table S1). The compressed aerogels display a minor decrease in surface area with increasing density, by ca. 10 % over the investigated density range. This indicates that the underlying CNF diameter remains unchanged for the concentrated samples, but some merging of CNF may occur during compression, consistent with the SEM data (Fig. 2b, e).  $D_{\text{pore,calc}}$  decreases from  $1290\text{ nm}$  to  $50\text{ nm}$  (Table S1) and the calculated total pore volumes ( $V_{\text{pore,calc}}$ ) is very large, up to  $181\text{ cm}^3\cdot\text{g}^{-1}$  for the lowest density aerogel ( $5.5\text{ mg}\cdot\text{cm}^{-3}$ ). The CNF aerogels are predominantly macroporous, particularly at low density where  $V_{\text{pore,BJH}}/V_{\text{pore,calc}}$  is less than 1 % and as a result, the average pore diameter calculated from nitrogen sorption,  $D_{\text{pore,calc}}$ , is not a true reflection of the real pore sizes.  $V_{\text{pore,BJH}}$  scatters substantially for the aerogels prepared by concentration, but there is a step in  $V_{\text{pore,BJH}}$  between concentrated and compressed samples, from  $1.0\text{--}1.5$  to  $1.5\text{--}2.3\text{ cm}^3\cdot\text{g}^{-1}$  respectively. This

jump indicates that densification through compression is more effective at increasing mesopore volume than densification through concentration.

Both the uncompressed and compressed aerogels were compressed from the baseline density of  $7\text{ mg}\cdot\text{cm}^{-3}$ , and therefore their difference is shown in the nitrogen sorption isotherms that display a type IV isotherm with hysteresis type H1 (Figs. S4–S6) (Sing & Williams, 2004). This type of isotherm indicates the presence of a smaller macropores and a large abundance of larger mesopores ( $20\text{--}50\text{ nm}$ ) (Lin & Jana, 2021; Sehaqui et al., 2011). The isotherms of the concentrated samples tend to be steeper at  $P/P_0 < 0.3$  due to the higher surface area, with higher equilibrium adsorption values between  $0.1$  and  $0.8 P/P_0$  as a result (Hu et al., 2000). The hysteresis area (Fig. 2h) is wider for compressed aerogels, which along with the pointed end, may indicate a larger fraction of mesopores (Liu et al., 1994). The BJH pore size distributions (Figs. 2i, S10) highlight the lower frequency of mesopores in the concentrated samples. In contrast, the compressed aerogels display a larger frequency of the pores in the  $20\text{--}40\text{ nm}$  region, a direct consequence of the densification that leads to a higher ratio of mesopores to macropores.

### 3.3. Mechanical properties

Fig. 3 shows typical stress-strain curves for cylindrical CNF aerogels of different densities. The decompression curves indicate that there is virtually no strain recovery and this was confirmed by measurements of the samples' height after a week of relaxation. As a result, the density of the recovered samples is directly proportional to the uniaxial strain to which each sample is compressed. For comparison, silica aerogels show a plastic limit but do recover about  $50\text{--}70\%$  of their initial height at low

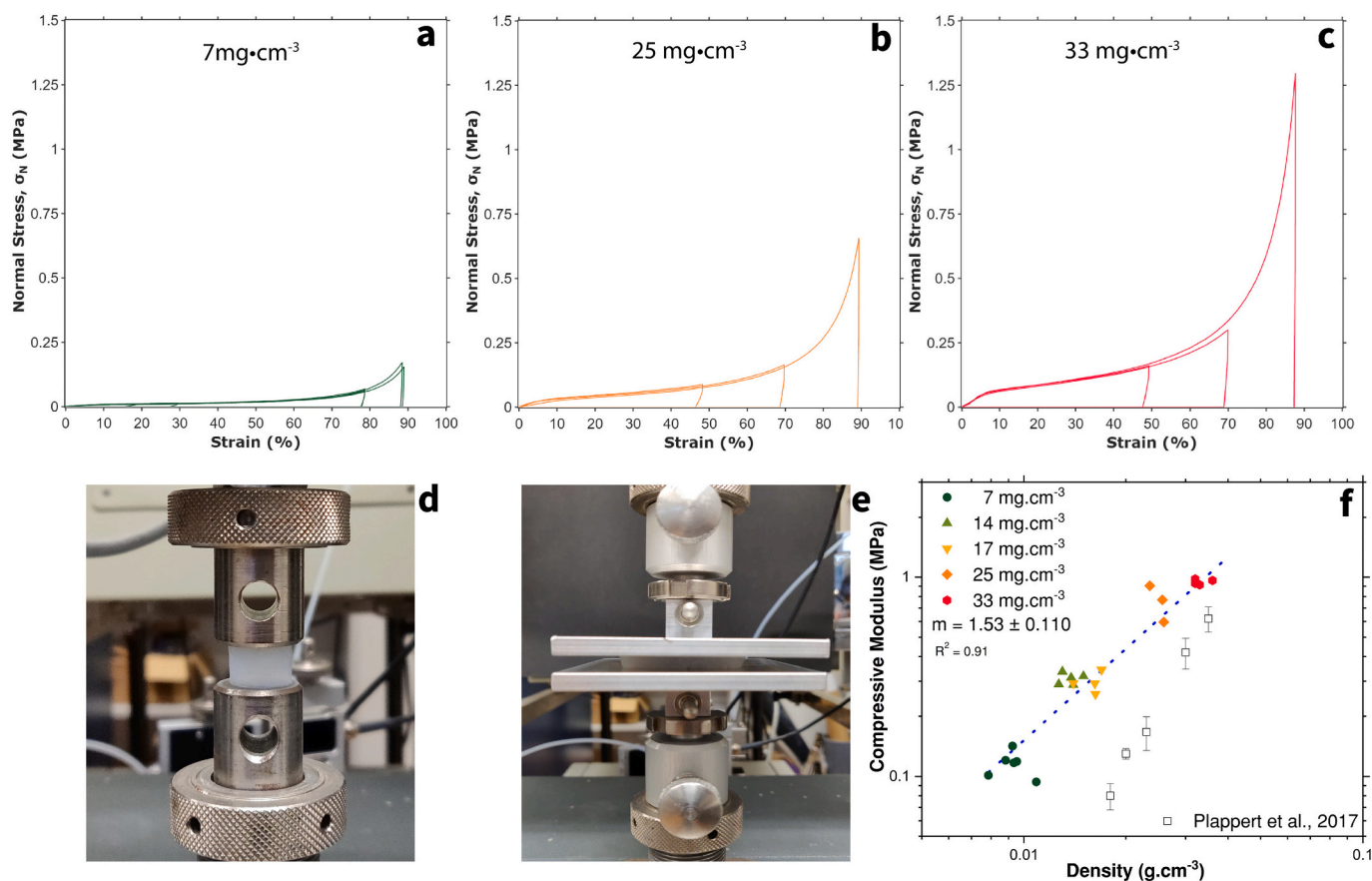


**Fig. 3.** a–c Uniaxial compression curves for samples of  $7$ ,  $25$ ,  $33\text{ mg}\cdot\text{cm}^{-3}$  densities respectively, d) image of cylindrical sample used during uniaxial compression (evidence of near zero Poisson's ratio), e) compression-densification for  $\lambda$  measurements, f) compressive E-modulus as a function of CNF aerogel density (cylinder samples; kept in  $\text{g}\cdot\text{cm}^{-3}$  for slope, which is characteristic for material).

density, and at higher densities recover a large fraction of their original volume after decompression (Sivaraman et al., 2021), as do some other elastic cellulose composites (Françon et al., 2020; Wong et al., 2015). The diameter of the cylinders did not change significantly after compression and decompression, i.e., the apparent Poisson's ratio is close to zero (Table S1).

Aerogels often have a power law dependence of the compressive modulus on density,  $E \propto \rho^\alpha$ , where  $E$  is the compressive modulus,  $\rho$  is the envelope density and  $\alpha$  is a material-dependent constant. The literature reports a large range of  $\alpha$  for cellulose aerogels, such as freeze-dried aerogels (1.8), foams (2.2) and simulation results (2.6) (Sehaqui et al., 2011; Srinivasa et al., 2017; Zhao et al., 2018). The variation could be a combination of aerogel drying protocols, pore network structure and other factors (Buchtová et al., 2019; Khlebnikov et al., 2020; Pircher et al., 2014, 2016). Our CNF aerogels have an  $\alpha$  value of  $1.53 \pm 0.11$ , which is considerably lower compared to CNF-SCD aerogels (2.95) (Plappert et al., 2017) but 50 % higher than 1.0 reported in the same density range (Kobayashi et al., 2014). Thus, although our CNF aerogels display a higher compressive modulus for a given density and the highest reported moduli for CNF-SCD aerogels (Fig. 3f), the rate of increase is lower. This different mechanical behavior is probably related to the different fibrillation processes (TEMPO-CNF v/s. dialdehyde modification (Plappert et al., 2017)), which leads to a finer degree of fibrillation of precursor materials and a finer network structure in the present study. The finer CNF may also explain the ability to reach a lower aerogel density.

### 3.4. Effect of density on thermal conductivity

Fig. 4 plots the density dependence of  $\lambda$  of CNF aerogels for an unprecedented range and resolution in density, highlighting lack of consensus in literature. The variation in  $\lambda$  can be explained by the equation for the overall thermal conductivity  $\lambda_{total}$ :

$$\lambda_{total} = \lambda_{conduction}^{solid} + \lambda_{conduction}^{gas} + \lambda_{convection}^{gas} + \lambda_{radiation} \quad (8)$$

At our measurement conditions (STP), radiative contributions,  $\lambda_{radiation}$ , are expected to be very low, with a negative dependence on density (Apostolopoulou-Kalkavoura et al., 2020; Collishaw & Evans, 1994). In the density range of the aerogels prepared from concentrated suspensions, the solid contributions,  $\lambda_{conduction}^{solid}$ , are expected to be very low due to the minimal amount of material present and the tortuous

network structure (Ebert, 2011). Convection,  $\lambda_{convection}^{gas}$ , is only a possible factor at the largest pore sizes ( $\geq 1 \mu\text{m}$ ) (Zou & Budtova, 2021). At low density,  $\lambda_{total}$  rapidly decreases with increasing density, e.g. from about 43 to 27  $\text{mW}\cdot\text{m}^{-1}\cdot\text{K}^{-1}$  for the aerogels prepared from concentrated suspensions. With the increase in density, the pore sizes rapidly decrease, which suppresses  $\lambda_{convection}^{gas}$ . In addition, there is most likely at least a partial suppression of  $\lambda_{conduction}^{gas}$  through the Knudsen effect toward the higher end of this density range, where the fraction of mesoporosity to the overall porosity starts to increase.

In this same low density regime (up to  $35 \text{ mg}\cdot\text{cm}^{-3}$ ), the compressed aerogels display a more rapid decrease in  $\lambda_{total}$  to values well below that of standing air, conclusive proof that  $\lambda_{conduction}^{gas}$  has been substantially suppressed, even at these relatively low densities. The lower  $\lambda_{total}$  for a given density of the compressed aerogels, correlates with the observed higher mesopore volume. Thus, even though the theoretical average pore size is the same, the higher fraction of mesoporosity for the compressed aerogels leads to a more effective suppression of  $\lambda_{conduction}^{gas}$  and as a consequence,  $\lambda_{total}$  (Reichenauer et al., 2007). We hypothesize that this difference in mesoporosity is the result of the preferential compression of local regions that are weaker, less dense and more macroporous. In addition to the change in mesoporosity, the compression may also induce the alignment of nanofibers, and hence also the pores, perpendicular to the direction of compression and heat flow.

Upon a further increase in density, an additional reduction in  $\lambda$  is observed, down to  $18.5 \text{ mW}\cdot\text{m}^{-1}\cdot\text{K}^{-1}$  at  $67 \text{ mg}\cdot\text{cm}^{-3}$ , which is the lowest measured value for our CNF aerogels, and a value that approaches the ultra-low thermal conductivities observed for commercial silica aerogel thermal superinsulation. Here,  $\lambda_{conduction}^{gas}$  is strongly suppressed by the Knudsen effect in the aerogel mesopores (Hemberger et al., 2009). Note that the estimated mesoporosity, approximated by  $V_{pore,BJH}/V_{pore,calc}$ , is still only on the order of 11 % for this sample, and we hypothesize that the effective reduction in  $\lambda_{total}$  is at least in part due to the alignment of the CNF and more effectively than an isotropic material. Beyond this optimum in density,  $\lambda_{total}$  increases with a further increase in density. As all other contributions are expected to decrease with increasing density, this increase must be due to an increase in  $\lambda_{conduction}^{solid}$  that is no longer fully compensated by concomitant reductions in  $\lambda_{conduction}^{gas}$ ,  $\lambda_{convection}^{gas}$  or  $\lambda_{radiation}$ . In summary, the thermal conductivity of CNF aerogels displays a U-shaped dependence of  $\lambda_{total}$  on density with a minimum at  $67 \text{ mg}\cdot\text{cm}^{-3}$ .

### 3.5. SAXS measurement and fiber alignment

In the compressed samples, CNF sheets form parallel to each other and perpendicular to the compression direction, and their frequency increases with the increase in density (Fig. 5) (Plappert, Nedelec, Renhofer, Lichtenegger, Bernstorff, and Liebner, 2018b). The SAXS data (Figs. 5, S8) in the XZ direction displays a rapidly increasing anisotropy with the increase in strain and density, evidenced by the increasingly ellipsoid nature of the 2D SAXS profiles. In addition to this increase in anisotropy, the overall scattering intensity increases, simply due to the presence of more CNF in the scattering volume for higher density samples. The same samples oriented in the XY direction display isotropic scattering for all densities tested which indicates that the fibers are randomly oriented in this plane. This is expected as the compression is uniaxial in the Z-axis, therefore the fibers in the XY plane remain 'unaligned'. Fig. S9 polar transforms the 2D SAXS profiles shown in Fig. 5a–e as a function of scattering vector modulus ( $\text{nm}^{-1}$ ) and azimuthal angle ( $^\circ$ ) and shows degree of orientation in parallel to the Y axis. The degree of orientation is quantified through the radial integration over a range in  $q$  of  $0.3\text{--}2.5 \text{ nm}^{-1}$  (Fig. 5f). The uncompressed sample ( $9 \text{ mg}\cdot\text{cm}^{-3}$ ) shows a constant integral value along the azimuthal angle (Fig. 5g), which confirms that there is little to no preferred orientation for an uncompressed sample. After compression to increasing strain values and densities, streak like signals at  $-90$  and  $+90^\circ$  indicate that there is greater frequency of scattering of CNF at a

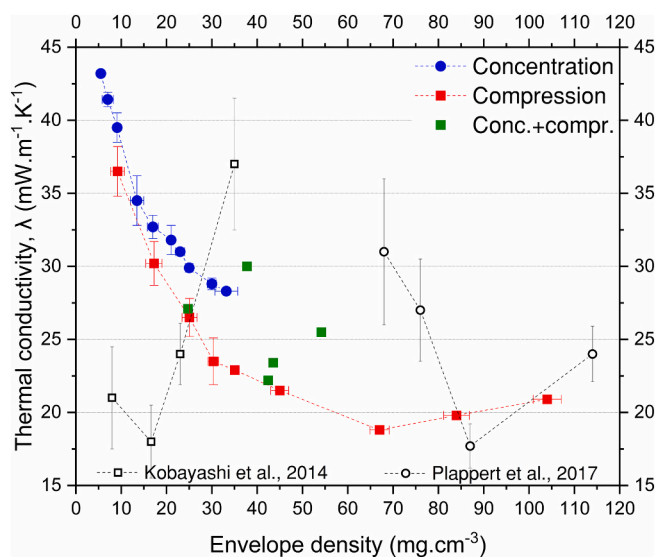
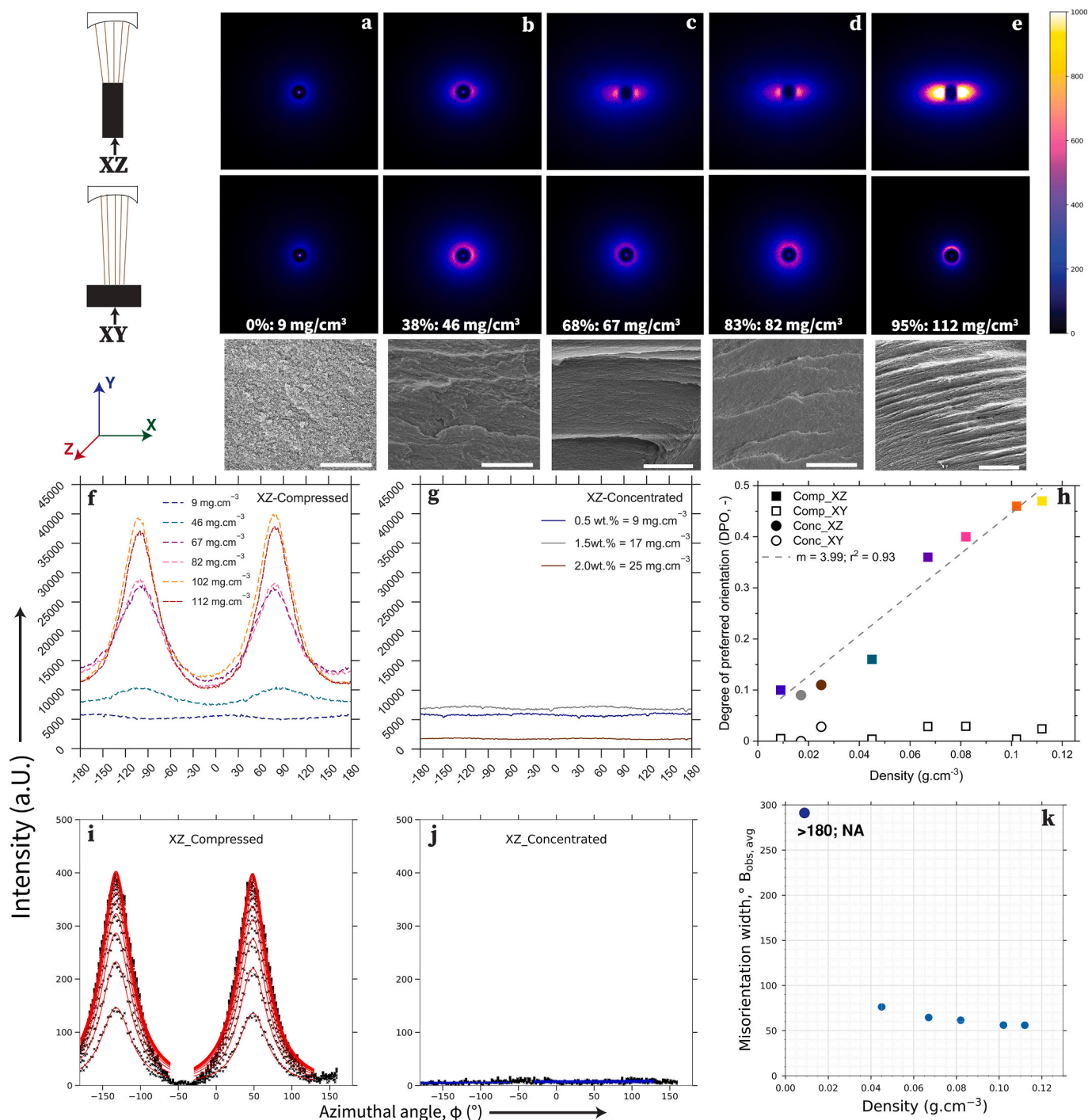


Fig. 4. Density dependence of thermal conductivity ( $\lambda$ ) for CNF aerogels. Lines are only guides to the eye. Open symbols are data from the literature. (Kobayashi et al., 2014; Plappert et al., 2017).



**Fig. 5.** a–e) 2D SAXS profiles and SEM images (scale bar of 50  $\mu\text{m}$ ) of CNF aerogels compressed to different densities. Color bar represents absolute values and is the same for all samples. The field of view covers a  $q$  range from 0 to  $2.5 \text{ nm}^{-1}$  (Pauw, 2013). f) Integrated SAXS intensity versus azimuthal angle measured in XZ orientation, g) integrated SAXS intensity versus azimuthal angle in XZ-axis orientation, h) degree of preferred orientation; i) Lorentzian fitted curves for the azimuthal profiles extracted for different  $q$ -ranges of  $0.3\text{--}1.1 \text{ nm}^{-1}$  with a step  $0.25 \text{ nm}^{-1}$  for the XZ-oriented concentrated sample and j) for the XZ-oriented concentrated sample. k) Ruland's misorientation width versus density (Ran et al., 2001; Ruland, 1969).

particular azimuthal angle, i.e. that fibers are aligned due to the uniaxial compression. With increasing density, the fibers are forced into a particular orientation as the intensity of the peaks increases as well as the ratio between the peak intensity to the baseline intensity (Rennhofer et al., 2019). The XZ orientation (Fig. 5f, i) contrasts with the XY orientation (Fig. S10g), where there are only minor variations in integrated intensity as a function of the azimuthal angle. The small variations that do occur indicate that there is a small degree of orientation in

the XY plane, independent of compression strain or density, presumably an artefact induced by pouring the viscous suspensions into the molds before gelation. The integrated SAXS data for the concentrated samples indicate that there is at most a small degree of alignment for both the XY and XZ directions (Figs. 5g, S10h).

We quantify the degree of alignment by three parameters, DPO (Fig. 5h), Herman's parameter (Fig. S10c) and the Ruland's misorientation width (Fig. 5k). The DPO and Herman's order parameter increase



linearly with increasing density for the XZ orientation that contrasts with the density-independent values near zero for the XY orientation. The misorientation width statistically quantifies our sample alignment for streak-like signal and the profile width is determinant of the fiber concentration at the peaks w.r.t. the entire SAXS profile. A perfectly aligned sample would attain a dirac-delta peak and would have a near-zero width. The higher width of the sample, the more it is misaligned and random (e.g.  $>180$  is not possible and labelled NA for  $9 \text{ mg}\cdot\text{cm}^{-3}$ ) and a lower number indicates higher degree of alignment (e.g. 50–70 after compression). This quantitatively confirms the SEM observations of the alignment of CNF in sheets perpendicular to the compression direction, and supports our interpretation of the thermal conductivity variations.

## 4. Discussion

### 4.1. Physics of thermal conductivity in CNF aerogels

An illustrative schematic that explains the decrease in pore size with density is shown in Fig. 6a. As density increases and the fibers start to align for the compressed samples (Fig. 5), the average pore size decreases and mesoporous fraction increases (Fig. 3d), which reduces  $\lambda$  in different stages (Fig. 6b). The first comprehensive dataset on the density

dependence of  $\lambda$  of CNF aerogels provided here, enables us to evaluate previous works on the topic (Fig. 4). The current data confirm the results from Plappert (Plappert et al., 2017), who reported a minimum  $\lambda$  of  $18 \text{ mW}\cdot\text{m}^{-1}\cdot\text{K}^{-1}$  at  $87 \text{ mg}\cdot\text{cm}^{-3}$ , i.e. close to our observed value. The shift of the minima may be related to differences in the CNF preparation protocols. In contrast, the data from Kobayashi (Kobayashi et al., 2014) are difficult to bring in line with our results as their reported minimum in  $\lambda$  of  $18 \text{ mW}\cdot\text{m}^{-1}\cdot\text{K}^{-1}$  requires a strong suppression of  $\lambda_{\text{conduction}}^{\text{gas}}$ . It is hard to explain how this can occur at a density of  $17 \text{ mg}\cdot\text{cm}^{-3}$ , where even  $\lambda_{\text{convection}}^{\text{gas}}$  may not be fully suppressed and a significant minimization of  $\lambda_{\text{conduction}}^{\text{gas}}$  through the Knudsen effect is difficult to imagine based on the expected pore sizes. In addition, it is difficult to rationalize why  $\lambda_{\text{total}}$  would increase so rapidly at densities between 17 and  $35 \text{ mg}\cdot\text{cm}^{-3}$ , particularly for a very fine network structure.

Our data on the CNF-SCD aerogels, with a minimum in thermal conductivity at  $67 \text{ mg}\cdot\text{cm}^{-3}$ , confirm the postulate that the density of biopolymer aerogels needs to be sufficiently high to reduce the thermal conductivity below that of standing air (Fig. 6c). Despite the large variability in chemistry and synthesis protocol, the thermal conductivities of biopolymer aerogels follow a clear pattern. Aside from just a few exceptions, biopolymer aerogels with thermal conductivities below  $20 \text{ mW}\cdot\text{m}^{-1}\cdot\text{K}^{-1}$  cluster around intermediate density values ( $100 \text{ mg}\cdot\text{cm}^{-3}$ ) and high surface areas ( $>250 \text{ m}^2\cdot\text{g}^{-1}$ ). The density range where the

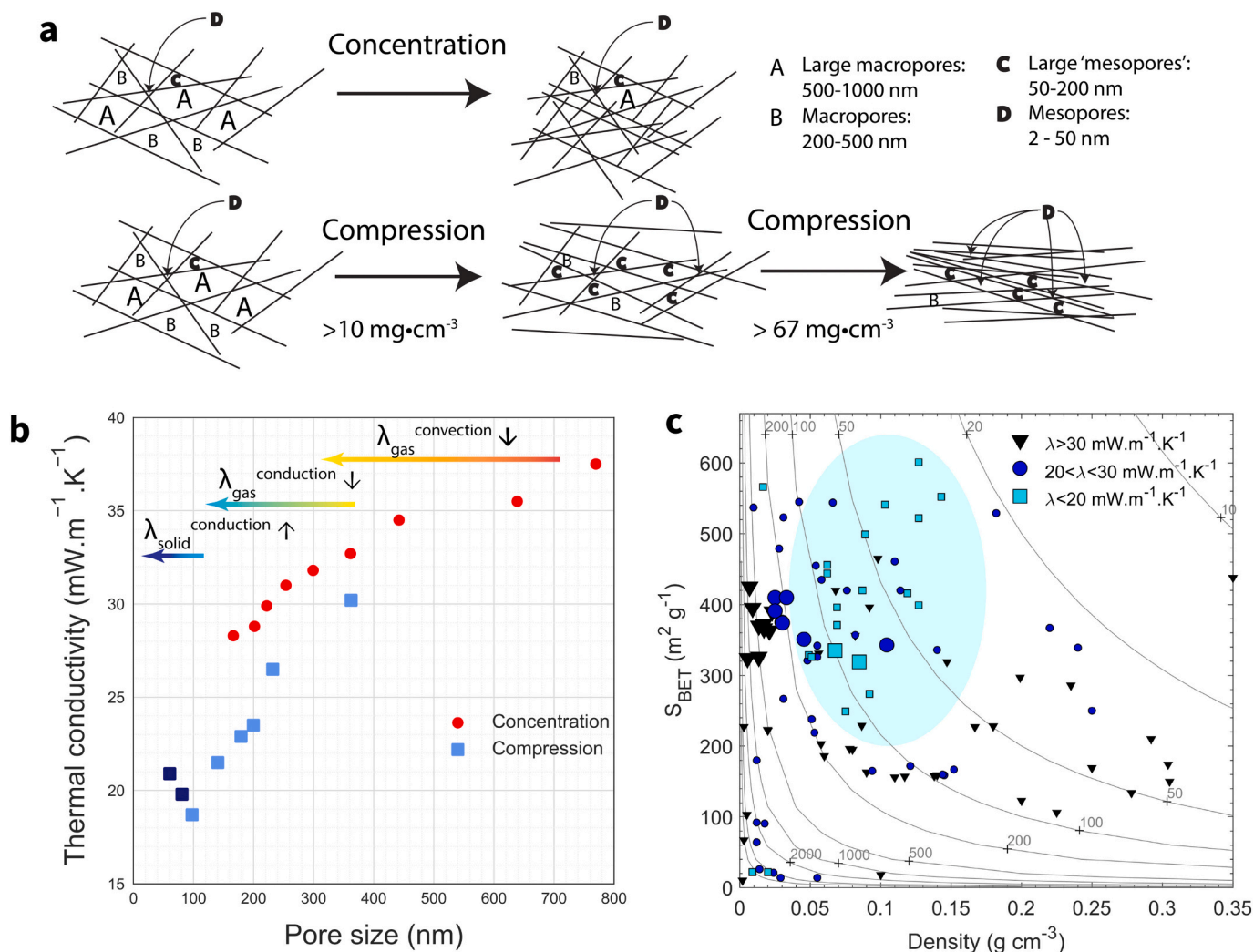


**Fig. 6.** a) Schematic illustration of fiber orientation and pore size changes with densification, b) dependence of thermal conductivity on pore size (calculated assuming hexagonal pores), c) thermal conductivity of biopolymer aerogels as a function of specific surface area and envelope density (kept in  $\text{g}\cdot\text{cm}^{-3}$  for ease of reading). Small markers denote data from the literature, compiled by (Guerrero-Alburquerque et al., 2020; Zhao et al., 2018), large markers denote the results from this study. The contours mark the theoretical pore diameter (in nm, assuming hexagonal pores,  $4\sqrt{V_{\text{pore}}}/\sqrt{(3)\cdot S_{\text{BET}}}$ ).

thermal conductivity is minimal is also similar to that of other aerogel materials. The minimum in  $\lambda$  at intermediate densities is to be expected as those are the conditions where the theoretical pore sizes (50–200 nm) are comparable to the mean free path length of the gas ( $\sim 70$  nm for air at STP) and thus small enough to reduce the gas phase conduction through the Knudsen effect. In addition, this density is low enough to limit the solid conduction through the aerogel backbone. With respect to the exceptions, in addition to the previously discussed Kobayashi data on CNF-SCD aerogels, three studies reported thermal conductivities below  $20 \text{ mW}\cdot\text{m}^{-1}\cdot\text{K}^{-1}$  for freeze-dried CNF aerogels at densities and surface areas below  $20 \text{ mg}\cdot\text{cm}^{-3}$  and  $25 \text{ m}^2\cdot\text{g}^{-1}$ , respectively, i.e. for pore sizes on the order of  $10 \mu\text{m}$  (Chen et al., 2014; Jiménez-Saelices et al., 2017; Wang et al., 2020). It is difficult to imagine a physical process that would reduce the thermal conductivity to such low values in these macroporous materials.

#### 4.2. CNF aerogel superinsulation for practical applications?

Our dataset and that from Plappert et al. (2017), indicate that the superinsulation region for CNF aerogels lies in the  $50\text{--}90 \text{ mg}\cdot\text{cm}^{-3}$  range (Fig. 5). These are still relatively low densities compared to other aerogel systems, but not low enough that the density becomes a unique selling point. Unlike commercially available hydrophobic silica aerogels, CNF aerogel, at present, is not market-ready. While compressed CNF-SCD aerogels do possess the required low  $\lambda$ , their production is not scalable as they are inefficient in their volumetric yield because of the difference between processed volume (gelation, solvent exchange, SCD) and the volume of the compressed final product. In contrast, freeze drying is potentially more scalable, but the resulting materials lack the desired mesoporosity and  $\lambda$ . Regardless of the processing protocol, cellulose aerogels are hydrophilic and special attention is required toward their long-term stability and/or hydrophobization. Recent research is focused on further improving the stability under real-world conditions (Plappert, Quraishi, Nedelec, Konnerth, Rennhofer, Lichtenegger, and Liebner, 2018a; Yamato et al., 2021). On the superinsulation side, the high performance and long term stability of silica aerogel products cannot yet be matched. Materials with moderate insulation performance, e.g. freeze-dried, hydrophobized CNF foams, have to compete with inexpensive biomass-based insulation products, e.g. straw and wood fiber boards. Thus, further academic and applied research needs to be conducted before CNF aerogel thermal insulation can enter the market, particularly to target higher stability, higher performance, and more resource effective production processes. Hybrids and composites in particular may pose a viable route to address these challenges.

## 5. Conclusion

This study uses TEMPO-oxidized CNF as a fundamental/model system and provides a detailed account of the effects of density, fiber orientation and pore size on the thermal conductivity of cellulose aerogels. The aerogels were prepared through a novel and simple hydrogel protocol that triggers gelation using acid vapors. This reproducible process yields transparent aerogels with high surface area and excellent mechanical properties. For the first time, the properties of CNF aerogels have been described over a very wide range in density, reached either by concentration or by compression. Our dataset shows that the thermal conductivity depends heavily on the density, but also on the densification strategy, with lower thermal conductivities for compressed aerogels due to the fiber alignment. Fiber alignment was mostly absent in the concentration based aerogels, as they achieve a more isotropic densification effect. The densification strategy based on concentration is limited by suspension viscosity to  $33 \text{ mg}\cdot\text{cm}^{-3}$  and  $28 \text{ mW}\cdot\text{m}^{-1}\cdot\text{K}^{-1}$  (roughly that of air). This is in contrast to compression based densification that yields a traditional U-shaped curve of  $\lambda$  and density with a minimum of  $18.5 \text{ mW}\cdot\text{m}^{-1}\cdot\text{K}^{-1}$  at  $67 \text{ mg}\cdot\text{cm}^{-3}$ . After the optimum value is reached, there was a slight increase in the  $\lambda$ , due to the increase in

solid conduction (thermal bridging). Our dataset confirms that the density dependence of the thermal conductivity of CNF aerogels does not deviate dramatically from that of other aerogel systems, and that a sufficiently high aerogel density is a necessary requirement for the production of super-insulating aerogels. This fundamental understanding of heat conduction in cellulose aerogels provides the basis to address the remaining challenges of long-term stability and process scalability, and paves the way to market-ready cellulose superinsulation products.

#### Data availability

Supplementary data is provided online. Raw data will be made available upon simple request to the corresponding authors. Scripts of the data analysis for SAXS are provided along with the raw data: [https://github.com/Deeptanshu-15/cellulose\\_aerogel\\_SAXS](https://github.com/Deeptanshu-15/cellulose_aerogel_SAXS).

#### CRediT authorship contribution statement

**Deeptanshu Sivaraman:** Conceptualization, Methodology, Software, Formal analysis, Investigation, Resources, Data curation, Writing – original draft, Writing – review & editing. **Gilberto Siqueira:** Conceptualization, Methodology, Writing – review & editing, Resources. **Anjani K. Maurya:** Writing – review & editing, Visualization, Resources, Methodology. **Shanyu Zhao:** Conceptualization, Methodology, Software, Formal analysis, Writing – review & editing. **Matthias M. Koebel:** Writing – review & editing, Supervision, Project administration. **Gustav Nyström:** Conceptualization, Methodology, Writing – review & editing, Resources. **Marco Lattuada:** Data curation, Writing – original draft, Supervision, Visualization, Project administration, Funding acquisition. **Wim J. Malfait:** Data curation, Writing – original draft, Investigation, Resources, Writing – review & editing, Supervision, Project administration, Funding acquisition.

#### Declaration of competing interest

The authors declare that they have no known competing financial interests or personal relationships that could have appeared to influence the work reported in this paper.

#### Acknowledgements

We acknowledge the contributions of Beatrice Fisher with the mechanical testing, and Zuzanna Kantor, Lukas Huber and Romain Civioc for their help with the aerogel characterization. We would also like to thank Dr. Michal Ganojak for his assistance in organizing the figures. This study was supported by the Swiss National Science Foundation through grant 200021\_179000 (W.J.M.).

#### Appendix A. Supplementary data

Supplementary data to this article can be found online at <https://doi.org/10.1016/j.carbpol.2022.119675>.

## References

- Abdul Khalil, H. P. S., Adnan, A. S., Yahya, E. B., Olaiya, N. G., Safrida, S., Hossain, M. S., Balakrishnan, V., Gopakumar, D. A., Abdullah, C. K., Oyekeani, A. A., & Pasquini, D. (2020). A review on plant cellulose nanofibre-based aerogels for biomedical applications. *Polymers*, 12(8), 1759. <https://doi.org/10.3390/polym12081759>
- Aeby, X., Poulin, A., Siqueira, G., Hausmann, M. K., & Nyström, G. (2021). Fully 3D printed and disposable paper supercapacitors. *Advanced Materials*, 33(26), 2101328. <https://doi.org/10.1002/adma.202101328>
- Aegerter, M. A., Leventis, N., & Koebel, M. M. (Eds.). (2011). *Aerogels handbook*. New York: Springer. <https://doi.org/10.1007/978-1-4419-7589-8>.
- Ahankari, S., Paliwal, P., Subhedar, A., & Kargarzadeh, H. (2021). Recent developments in nanocellulose-based aerogels in thermal applications: A review. *ACS Nano*, 15(3), 3849–3874. <https://doi.org/10.1021/acsnano.0c09678>
- Alam, M., Singh, H., & Limbachiya, M. C. (2011). Vacuum insulation panels (VIPs) for building construction industry – A review of the contemporary developments and

- future directions. *Applied Energy*, 88(11), 3592–3602. <https://doi.org/10.1016/j.apenergy.2011.04.040>
- Apostolopoulou-Kalkavoura, V., Munier, P., & Bergström, L. (2020). Thermally insulating nanocellulose-based materials. *Advanced Materials*, 2001839. <https://doi.org/10.1002/adma.202001839>. n/a(n/a).
- Arcari, M., Zuccarella, E., Axelrod, R., Adamcik, J., Sánchez-Ferrer, A., Mezzenga, R., & Nyström, G. (2019). Nanostructural properties and twist periodicity of cellulose nanofibrils with variable charge density. *Biomacromolecules*, 20(3), 1288–1296. <https://doi.org/10.1021/acs.biomac.8b01706>
- Baudron, V., Gurikov, P., Smirnova, I., & Whitehouse, S. (2019). Porous starch materials via supercritical- and freeze-drying. *Gels*, 5(1), 12. <https://doi.org/10.3390/gels5010012>
- Berglund, L., Nissilä, T., Sivaraman, D., Komulainen, S., Telkki, V.-V., & Oksman, K. (2021). Seaweed-derived alginate-cellulose nanofiber aerogel for insulation applications. *ACS Applied Materials & Interfaces*, Article acsami.1c07954. <https://doi.org/10.1021/acsami.1c07954>
- Buchtová, N., Pradille, C., Bouvard, J.-L., & Budtova, T. (2019). Mechanical properties of cellulose aerogels and cryogels. *Soft Matter*, 15(39), 7901–7908. <https://doi.org/10.1039/C9SM01028A>
- Chen, W., Li, Q., Wang, Y., Yi, X., Zeng, J., Yu, H., Liu, Y., & Li, J. (2014). Comparative study of aerogels obtained from differently prepared nanocellulose fibers. *ChemSusChem*, 7(1), 154–161. <https://doi.org/10.1002/cssc.201300950>
- Chu, Y., Sun, Y., Wu, W., & Xiao, H. (2020). Dispersion properties of nanocellulose: A review. *Carbohydrate Polymers*, 250, Article 116892. <https://doi.org/10.1016/j.carbpol.2020.116892>
- Collishaw, P. G., & Evans, J. R. G. (1994). An assessment of expressions for the apparent thermal conductivity of cellular materials. *Journal of Materials Science*, 29(9), 2261–2273. <https://doi.org/10.1007/BF00363413>
- Dri, F. L., Shang, S., Hector, L. G., Saxe, P., Liu, Z.-K., Moon, R. J., & Zavattieri, P. D. (2014). Anisotropy and temperature dependence of structural, thermodynamic, and elastic properties of crystalline cellulose I $\beta$ : A first-principles investigation. *Modelling and Simulation in Materials Science and Engineering*, 22(8), Article 085012. <https://doi.org/10.1088/0965-0393/22/8/085012>
- Ebert, H.-P. (2011). Thermal properties of aerogels. In M. A. Aegerter, N. Leventis, & M. M. Koebel (Eds.), *Aerogels handbook* (pp. 537–564). Springer. [https://doi.org/10.1007/978-1-4419-7589-8\\_23](https://doi.org/10.1007/978-1-4419-7589-8_23)
- Fourmann, O., Hausmann, M. K., Neels, A., Schubert, M., Nyström, G., Zimmermann, T., & Siqueira, G. (2021). 3D printing of shape-morphing and antibacterial anisotropic nanocellulose hydrogels. *Carbohydrate Polymers*, 259, Article 117716. <https://doi.org/10.1016/j.carbpol.2021.117716>
- Françon, H., Wang, Z., Marais, A., Mystek, K., Piper, A., Granberg, H., Malti, A., Gatenholm, P., Larsson, P. A., & Wågberg, L. (2020). Ambient-dried, 3D-printable and electrically conducting cellulose nanofiber aerogels by inclusion of functional polymers. *Advanced Functional Materials*, 30(12), 1909383. <https://doi.org/10.1002/adfm.201909383>
- Fricke, J., Lu, X., Wang, P., Büttner, D., & Heinemann, U. (1992). Optimization of monolithic silica aerogel insulants. *International Journal of Heat and Mass Transfer*, 35(9), 2305–2309. [https://doi.org/10.1016/0017-9310\(92\)90073-2](https://doi.org/10.1016/0017-9310(92)90073-2)
- García-González, C. A., Budtova, T., Durães, L., Erkey, C., Del Gaudio, P., Gurikov, P., Koebel, M., Liebner, F., Neagu, M., & Smirnova, I. (2019). An opinion paper on aerogels for biomedical and environmental applications. *Molecules*, 24(9), 1815. <https://doi.org/10.3390/molecules24091815>
- Gavillon, R., & Budtova, T. (2008). Aerocellulose: New highly porous cellulose prepared from cellulose–NaOH aqueous solutions. *Biomacromolecules*, 9(1), 269–277. <https://doi.org/10.1021/bm700972k>
- Groult, S., & Budtova, T. (2018). Thermal conductivity/structure correlations in thermal super-insulating pectin aerogels. *Carbohydrate Polymers*, 196, 73–81. <https://doi.org/10.1016/j.carbpol.2018.05.026>
- Guerrero-Albuquerque, N., Zhao, S., Adilien, N., Koebel, M. M., Lattuada, M., & Malfait, W. J. (2020). Strong, machinable, and insulating chitosan-urea aerogels: Toward ambient pressure drying of biopolymer aerogel monoliths. *ACS Applied Materials & Interfaces*, 12(19), 22037–22049. <https://doi.org/10.1021/acsami.0c03047>
- Gurikov, P. S. P. R., Griffin, J. S., Steiner, S. A., III, & Smirnova, I. (2019). Solvent exchange in the processing of biopolymer aerogels: Current status and open questions. *Industrial & Engineering Chemistry Research*. <https://doi.org/10.1021/acs.iecr.9b02967>
- Hammerschmidt, U. (2002). Guarded Hot-Plate (GHP) method: Uncertainty assessment. *International Journal of Thermophysics*, 23(6), 1551–1570. <https://doi.org/10.1023/A:1020737900473>
- Heinze, T., El Seoud, O. A., & Koschella, A. (2018). Production and characteristics of cellulose from different sources. In T. Heinze, O. A. El Seoud, & A. Koschella (Eds.), *Cellulose derivatives: Synthesis, structure, and properties* (pp. 1–38). Springer International Publishing. [https://doi.org/10.1007/978-3-319-73168-1\\_1](https://doi.org/10.1007/978-3-319-73168-1_1)
- Hemmerger, F., Weis, S., Reichenauer, G., & Ebert, H.-P. (2009). Thermal transport properties of functionally graded carbon aerogels. *International Journal of Thermophysics*, 30(4), 1357–1371. <https://doi.org/10.1007/s10765-009-0616-0>
- Hoepfner, S., Ratke, L., & Milow, B. (2008). Synthesis and characterisation of nanofibrillar cellulose aerogels. *Cellulose*, 15(1), 121–129. <https://doi.org/10.1007/s10570-007-9146-8>
- Hon, D. N.-S. (1995). *Chemical modification of lignocellulosic materials*. CRC Press.
- Hu, Z., Srinivasan, M. P., & Ni, Y. (2000). Preparation of mesoporous high-surface-area activated carbon. *Advanced Materials*, 12(1), 62–65. [https://doi.org/10.1002/\(SICI\)1521-4095\(200001\)12:1<62::AID-ADMA62>3.0.CO;2-B](https://doi.org/10.1002/(SICI)1521-4095(200001)12:1<62::AID-ADMA62>3.0.CO;2-B)
- Hüsing, N., & Schubert, U. (1998). Aerogels—Airy materials: Chemistry, structure, and properties. *Angewandte Chemie International Edition*, 37(1–2), 22–45. [https://doi.org/10.1002/\(SICI\)1521-3773\(19980202\)37:1/2<22::AID-ANIE22>3.0.CO;2-I](https://doi.org/10.1002/(SICI)1521-3773(19980202)37:1/2<22::AID-ANIE22>3.0.CO;2-I)
- Innerlohinger, J., Weber, H. K., & Kraft, G. (2006). Aerocellulose: Aerogels and aerogel-like materials made from cellulose. *Macromolecular Symposia*, 244(1), 126–135. <https://doi.org/10.1002/masy.200651212>
- Isogai, A., Saito, T., & Fukuzumi, H. (2011). TEMPO-oxidized cellulose nanofibers. *Nanoscale*, 3(1), 71–85. <https://doi.org/10.1039/C0NR00583E>
- Iswar, S., Galmari, S., Bonanomi, L., Wernery, J., Roumeli, E., Nimalshantha, S., Ben Ishai, A. M., Lattuada, M., Koebel, M. M., & Malfait, W. J. (2021). Dense and strong, but superinsulating silica aerogel. *Acta Materialia*, 213, Article 116959. <https://doi.org/10.1016/j.actamat.2021.116959>
- Jiménez-Saelices, C., Seantier, B., Cathala, B., & Grohens, Y. (2017). Spray freeze-dried nanofibrillated cellulose aerogels with thermal superinsulating properties. *Carbohydrate Polymers*, 157, 105–113. <https://doi.org/10.1016/j.carbpol.2016.09.068>
- Jin, H., Nishiyama, Y., Wada, M., & Kuga, S. (2004). Nanofibrillar cellulose aerogels. *Colloids and Surfaces A: Physicochemical and Engineering Aspects*, 240(1), 63–67. <https://doi.org/10.1016/j.colsurfa.2004.03.007>
- Johansson, L.-S., Tammelin, T., Campbell, J. M., Setälä, H., & Österberg, M. (2011). Experimental evidence on medium driven cellulose surface adaptation demonstrated using nanofibrillated cellulose. *Soft Matter*, 7(22), 10917–10924. <https://doi.org/10.1039/C1SM06073B>
- Kamide, K. (2005). *Cellulose and cellulose derivatives*. Elsevier.
- Khlebnikov, O. N., Postnova, I. V., Chen, L.-J., & Shchipunov, Y. A. (2020). Silication of dimensionally stable cellulose aerogels for improving their mechanical properties. *Colloid Journal*, 82(4), 448–459. <https://doi.org/10.1134/S1061933X20040043>
- Kieffer, J., & Wright, J. P. (2013). PyFAI: A python library for high performance azimuthal integration on GPU. *Powder Diffraction*, 28(S2), S339–S350. <https://doi.org/10.1017/S0885715613000924>
- Kistler, S. S. (1931). Coherent expanded aerogels and jellies. *Nature*, 127(3211). <https://doi.org/10.1038/127741a0>, 741–741.
- Knudsen, E. B., Sørensen, H. O., Wright, J. P., Goret, G., & Kieffer, J. (2013). FabIO: Easy access to two-dimensional X-ray detector images in python. *Journal of Applied Crystallography*, 46(2), 537–539. <https://doi.org/10.1107/S0021889813000150>
- Kobayashi, Y., Saito, T., & Isogai, A. (2014). Aerogels with 3D ordered nanofiber skeletons of liquid-crystalline nanocellulose derivatives as tough and transparent insulators. *Angewandte Chemie International Edition*, 53(39), 10394–10397. <https://doi.org/10.1002/anie.201405123>
- Koebel, M., Rigacci, A., & Achard, P. (2012). Aerogel-based thermal superinsulation: An overview. *Journal of Sol-Gel Science and Technology*, 63(3), 315–339. <https://doi.org/10.1007/s10971-012-2792-9>
- Lee, J.-H., Hamm, S.-Y., Cheong, J.-Y., Kim, H.-S., Ko, E.-J., Lee, K.-S., & Lee, S.-I. (2009). Characterizing riverbank-filtered water and river water qualities at a site in the lower Nakdong River basin, Republic of Korea. *Journal of Hydrology*, 376(1), 209–220. <https://doi.org/10.1016/j.jhydrol.2009.07.030>
- Liebner, F., Potthast, A., Rosenau, T., Haimer, E., & Wendland, M. (2008). In 62(2). *Cellulose aerogels: Highly porous, ultra-lightweight materials* (pp. 129–135). <https://doi.org/10.1515/HF.2008.051>
- Lin, W.-H., & Jana, S. C. (2021). Analysis of porous structures of cellulose aerogel monoliths and microparticles. *Microporous and Mesoporous Materials*, 310, Article 110625. <https://doi.org/10.1016/j.micromeso.2020.110625>
- Liu, H., Zhang, L., & Seaton, N. A. (1994). Characterisation of mesoporous solids using sorption hysteresis measurements. In J. Rouquerol, F. Rodríguez-Reinoso, K. S. W. Sing, & K. K. Unger (Eds.), *Studies in surface science and catalysis* (Vol. 87, pp. 129–139). Elsevier. [https://doi.org/10.1016/S0167-2991\(08\)63072-4](https://doi.org/10.1016/S0167-2991(08)63072-4)
- Lu, X., Arduini-Schuster, M. C., Kuhn, J., Nilsson, O., Fricke, J., & Pekala, R. W. (1992). Thermal conductivity of monolithic organic aerogels. *Science*, 255(5047), 971–972. <https://doi.org/10.1126/science.255.5047.971>
- Lu, X., Wang, P., Arduini-Schuster, M. C., Kuhn, J., Büttner, D., Nilsson, O., Heinemann, U., & Fricke, J. (1992). Thermal transport in organic and opacified silica monolithic aerogels. *Journal of Non-Crystalline Solids*, 145, 207–210. [https://doi.org/10.1016/S0022-3093\(05\)80457-0](https://doi.org/10.1016/S0022-3093(05)80457-0)
- Maciel, M. M. A. D., Benini, K. C. C. d. C., Voorwald, H. J. C., & Cioffi, M. O. H. (2019). Obtainment and characterization of nanocellulose from an unwoven industrial textile cotton waste: Effect of acid hydrolysis conditions. *International Journal of Biological Macromolecules*, 126, 496–506. <https://doi.org/10.1016/j.ijbiomac.2018.12.020>
- Mandal, C., Donthula, S., Rewatkar, P. M., Sotiriou-Leventis, C., & Leventis, N. (2019). Experimental deconvolution of depressurization from capillary shrinkage during drying of silica wet-gels with SCF CO<sub>2</sub> why aerogels shrink? *Journal of Sol-Gel Science and Technology*, 92(3), 662–680. <https://doi.org/10.1007/s10971-019-05124-x>
- Mathew, A. P., Chakraborty, A., Oksman, K., & Sain, M. (2006). The structure and mechanical properties of cellulose nanocomposites prepared by twin screw extrusion. In Vol. 938. *Cellulose nanocomposites* (pp. 114–131). American Chemical Society. <https://doi.org/10.1021/bk-2006-0938.ch009>
- Mauray, A. K., Parrilli, A., Kochetkova, T., Schwiedrzik, J., Dommann, A., & Neels, A. (2021). Multiscale and multimodal X-ray analysis: Quantifying phase orientation and morphology of mineralized turkey leg tendons. *Acta Biomaterialia*, 129, 169–177. <https://doi.org/10.1016/j.actbio.2021.05.022>
- Nascimento, J. H. O. d., Luz, R. F., Galvão, F. M. F., Melo, J. D. D., Oliveira, F. R., Ladchumananandasivam, R., & Zille, A. (2015). Extraction and characterization of cellulosic nanowhisker obtained from discarded cotton fibers. *Materials Today: Proceedings*, 2(1), 1–7. <https://doi.org/10.1016/j.matpr.2015.04.001>



- Newville, M., Stensitzki, T., Allen, D. B., & Ingargiola, A. (2014). LMFIT: Non-linear least-square minimization and curve-fitting for python. *Zenodo*. <https://doi.org/10.5281/zenodo.11813>
- Nordenström, M., Fall, A., Nyström, G., & Wågberg, L. (2017). Formation of colloidal nanocellulose glasses and gels. *Langmuir*, 33(38), 9772–9780. <https://doi.org/10.1021/acs.langmuir.7b01832>
- Pauw, B. R. (2013). Everything SAXS: Small-angle scattering pattern collection and correction. *Journal of Physics: Condensed Matter*, 25(38), Article 383201. <https://doi.org/10.1088/0953-8984/25/38/383201>
- Pircher, N., Veigel, S., Aigner, N., Nedelec, J. M., Rosenau, T., & Liebner, F. (2014). Reinforcement of bacterial cellulose aerogels with biocompatible polymers. *Carbohydrate Polymers*, 111, 505–513. <https://doi.org/10.1016/j.carbpol.2014.04.029>
- Pircher, N., Carbajal, L., Schimper, C., Bacher, M., Rennhofer, H., Nedelec, J.-M., Lichtenegger, H. C., Rosenau, T., & Liebner, F. (2016). Impact of selected solvent systems on the pore and solid structure of cellulose aerogels. *Cellulose*, 23(3), 1949–1966. <https://doi.org/10.1007/s10570-016-0896-z>
- Plappert, S. F., Nedelec, J.-M., Rennhofer, H., Lichtenegger, H. C., & Liebner, F. W. (2017). Strain hardening and pore size harmonization by uniaxial densification: A facile approach toward superinsulating aerogels from nematic nanofibrillated 2,3-dicarboxyl cellulose. *Chemistry of Materials*, 29(16), 6630–6641. <https://doi.org/10.1021/acs.chemmater.7b00787>
- Plappert, S. F., Nedelec, J.-M., Rennhofer, H., Lichtenegger, H. C., Bernstorff, S., & Liebner, F. W. (2018). Self-assembly of cellulose in super-cooled ionic liquid under the impact of decelerated antisolvent infusion: An approach toward anisotropic gels and aerogels. *Biomacromolecules*, 19(11), 4411–4422. <https://doi.org/10.1021/acs.biomac.8b01278>
- Plappert, S. F., Quraishi, S., Nedelec, J.-M., Konnerth, J., Rennhofer, H., Lichtenegger, H. C., & Liebner, F. W. (2018). Conformal ultrathin coating by scCO<sub>2</sub>-mediated PMMA deposition: A facile approach to add moisture resistance to lightweight ordered nanocellulose aerogels. *Chemistry of Materials*, 30(7), 2322–2330. <https://doi.org/10.1021/acs.chemmater.7b05226>
- Putz, F., Morak, R., Elsaesser, M. S., Balzer, C., Braxmeier, S., Bernardi, J., Paris, O., Reichenauer, G., & Hüsing, N. (2017). Setting directions: Anisotropy in hierarchically organized porous silica. *Chemistry of Materials*, 29(18), 7969–7975. <https://doi.org/10.1021/acs.chemmater.7b03032>
- Qian, C., Li, L., Gao, M., Yang, H., Cai, Z., Chen, B., Xiang, Z., Zhang, Z., & Song, Y. (2019). All-printed 3D hierarchically structured cellulose aerogel based triboelectric nanogenerator for multi-functional sensors. *Nano Energy*, 63, Article 103885. <https://doi.org/10.1016/j.nanoen.2019.103885>
- Raman, S. P., Gurikov, P., & Smirnova, I. (2015). Hybrid alginate based aerogels by carbon dioxide induced gelation: Novel technique for multiple applications. *The Journal of Supercritical Fluids*, 106, 23–33. <https://doi.org/10.1016/j.supflu.2015.05.003>
- Ran, S., Fang, D., Zong, X., Hsiao, B. S., Chu, B., & Cuniff, P. M. (2001). Structural changes during deformation of Kevlar fibers via on-line synchrotron SAXS/WAXD techniques. *Polymer*, 42(4), 1601–1612. [https://doi.org/10.1016/S0032-3861\(00\)00460-2](https://doi.org/10.1016/S0032-3861(00)00460-2)
- Reichenauer, G., Heinemann, U., & Ebert, H.-P. (2007). Relationship between pore size and the gas pressure dependence of the gaseous thermal conductivity. *Colloids and Surfaces A: Physicochemical and Engineering Aspects*, 300(1), 204–210. <https://doi.org/10.1016/j.colsurfa.2007.01.020>
- Rennhofer, H., Plappert, S. F., Lichtenegger, H. C., Bernstorff, S., Fitzka, M., Nedelec, J.-M., & Liebner, F. W. (2019). Matter into the nanostructure of anisotropic cellulose aerogels upon compression. *Soft Matter*, 15(41), 8372–8380. <https://doi.org/10.1039/C9SM01422E>
- Rhim, J.-W., & Ng, P. K. W. (2007). Natural biopolymer-based nanocomposite films for packaging applications. *Critical Reviews in Food Science and Nutrition*, 47(4), 411–433. <https://doi.org/10.1080/10408390600846366>
- Rudaz, C., Courson, R., Bonnet, L., Calas-Etienne, S., Sallée, H., & Budtova, T. (2014). Aeropectin: Fully biomass-based mechanically strong and thermal superinsulating aerogel. *Biomacromolecules*, 15(6), 2188–2195. <https://doi.org/10.1021/bm500345u>
- Ruland, W. (1969). Small-angle scattering studies on carbonized cellulose fibers. *Journal of Polymer Science Part C: Polymer Symposia*, 28(1), 143–151. <https://doi.org/10.1002/polc.5070280113>
- Saxe, F., Eder, M., Benecke, G., Aichmayer, B., Fratzl, P., Burgert, I., & Rüggeberg, M. (2014). Measuring the distribution of cellulose microfibril angles in primary cell walls by small angle X-ray scattering. *Plant Methods*, 10, 25. <https://doi.org/10.1186/1746-4811-10-25>
- Seantier, B., Bendahou, D., Bendahou, A., Grohens, Y., & Kaddami, H. (2016). Multi-scale cellulose based new bio-aerogel composites with thermal super-insulating and tunable mechanical properties. *Carbohydrate Polymers*, 138, 335–348. <https://doi.org/10.1016/j.carbpol.2015.11.032>
- Sehaqui, H., Zhou, Q., & Berglund, L. A. (2011). High-porosity aerogels of high specific surface area prepared from nanofibrillated cellulose (NFC). *Composites Science and Technology*, 71(13), 1593–1599. <https://doi.org/10.1016/j.compscitech.2011.07.003>
- Sing, K. S. W., & Williams, R. T. (2004). Physisorption hysteresis loops and the characterization of nanoporous materials. *Adsorption Science & Technology*, 22(10), 773–782. <https://doi.org/10.1260/0263617053499032>
- Siqueira, G., Kokkinis, D., Libanori, R., Hausmann, M. K., Gladman, A. S., Neels, A., Tingaut, P., Zimmermann, T., Lewis, J. A., & Studart, A. R. (2017). Cellulose nanocrystal inks for 3D printing of textured cellular architectures. *Advanced Functional Materials*, 27(12), 1604619. <https://doi.org/10.1002/adfm.201604619>
- Sivaraman, D., Zhao, S., Iswar, S., Lattuada, M., & Malfait, W. J. (2021). Aerogel spring-back correlates with strain recovery: Effect of silica concentration and aging. *Advanced Engineering Materials*, 2100376. <https://doi.org/10.1002/adem.202100376>. n/a(n/a).
- Srinivasa, P., Kulachenko, A., & Karlberg, F. (2017). Material properties of the cell walls in nanofibrillar cellulose foams from finite element modelling of tomography scans. *Cellulose*, 24(2), 519–533. <https://doi.org/10.1007/s10570-016-1179-4>
- Stahl, T., Brunner, S., Zimmermann, M., & Ghazi Wakili, K. (2012). Thermo-hygric properties of a newly developed aerogel based insulation rendering for both exterior and interior applications. *Energy and Buildings*, 44, 114–117. <https://doi.org/10.1016/j.enbuild.2011.09.041>
- Sun, Y., Chu, Y., Wu, W., & Xiao, H. (2021). Nanocellulose-based lightweight porous materials: A review. *Carbohydrate Polymers*, 255, Article 117489. <https://doi.org/10.1016/j.carbpol.2020.117489>
- Takeshita, S., Sadeghpour, A., Sivaraman, D., Zhao, S., & Malfait, W. J. (2020). Solvents, CO<sub>2</sub> and biopolymers: Structure formation in chitosan aerogel. *Carbohydrate Polymers*, 247, Article 116680. <https://doi.org/10.1016/j.carbpol.2020.116680>
- Vareda, J. P., Valente, A. J. M., & Duraes, L. (2016). Heavy metals in Iberian soils: Removal by current adsorbents/amendments and prospective for aerogels. *Advances in Colloid and Interface Science*, 237, 28–42. <https://doi.org/10.1016/j.cis.2016.08.009>
- Wang, Z. (2019). Recent advances in novel metallic honeycomb structure. *Composites Part B: Engineering*, 166, 731–741. <https://doi.org/10.1016/j.compositesb.2019.02.011>
- Wang, D., Peng, H., Yu, B., Zhou, K., Pan, H., Zhang, L., Li, M., Liu, M., Tian, A., & Fu, S. (2020). Biomimetic structural cellulose nanofiber aerogels with exceptional mechanical, flame-retardant and thermal-insulating properties. *Chemical Engineering Journal*, 389, Article 124449. <https://doi.org/10.1016/j.cej.2020.124449>
- Weishaupt, R., Siqueira, G., Schubert, M., Tingaut, P., Maniura-Weber, K., Zimmermann, T., Thöny-Meyer, L., Faccio, G., & Ihssen, J. (2015). TEMPO-oxidized nanofibrillated cellulose as a high density carrier for bioactive molecules. *Biomacromolecules*, 16(11), 3640–3650. <https://doi.org/10.1021/acs.biomac.5b01100>
- Wong, J. C. H., Kaymak, H., Brunner, S., & Koebel, M. M. (2014). Mechanical properties of monolithic silica aerogels made from polyethoxydisiloxanes. *Microporous and Mesoporous Materials*, 183, 23–29. <https://doi.org/10.1016/j.micromeso.2013.08.029>
- Wong, J. C. H., Kaymak, H., Tingaut, P., Brunner, S., & Koebel, M. M. (2015). Mechanical and thermal properties of nanofibrillated cellulose reinforced silica aerogel composites. *Microporous and Mesoporous Materials*, 217, 150–158. <https://doi.org/10.1016/j.micromeso.2015.06.025>
- Wu, T., Zeng, Z., Siqueira, G., De France, K., Sivaraman, D., Schreiner, C., Figi, R., Zhang, Q., & Nyström, G. (2020). Dual-porous cellulose nanofibril aerogels via modular drying and cross-linking. *Nanoscale*, 12(13), 7383–7394. <https://doi.org/10.1039/D0NR00860E>
- Yamato, K., Yoshida, Y., Kumamoto, Y., & Isogai, A. (2021). Surface modification of TEMPO-oxidized cellulose nanofibers, and properties of their acrylate and epoxy resin composite films. *Cellulose*. <https://doi.org/10.1007/s10570-021-04131-y>
- Zhang, Q., Yang, X., Li, P., Huang, G., Feng, S., Shen, C., Han, B., Zhang, X., Jin, F., Xu, F., & Lu, T. J. (2015). Bioinspired engineering of honeycomb structure – Using nature to inspire human innovation. *Progress in Materials Science*, 74, 332–400. <https://doi.org/10.1016/j.pmatsci.2015.05.001>
- Zhao, S., Zhang, Z., Sèbe, G., Wu, R., Virtudazo, R. V. R., Tingaut, P., & Koebel, M. M. (2015). Multiscale assembly of superinsulating silica aerogels within silylated nanocellulosic scaffolds: Improved mechanical properties promoted by nanoscale chemical compatibilization. *Advanced Functional Materials*, 25(15), 2326–2334. <https://doi.org/10.1002/adfm.201404368>
- Zhao, S., Malfait, W. J., Guerrero-Alburquerque, N., Koebel, M. M., & Nyström, G. (2018). Biopolymer aerogels and foams: Chemistry, properties, and applications. *Angewandte Chemie International Edition*, 57(26), 7580–7608. <https://doi.org/10.1002/anie.201709014>
- Zhao, S., Siqueira, G., Drdova, S., Norris, D., Ubert, C., Bonnin, A., Galmarini, S., Ganobjak, M., Pan, Z., Brunner, S., Nyström, G., Wang, J., Koebel, M. M., & Malfait, W. J. (2020). Additive manufacturing of silica aerogels. *Nature*, 584(7821), 387–392. <https://doi.org/10.1038/s41586-020-2594-0>
- Zhu, Z., Snellings, G. M. B. F., Koebel, M. M., & Malfait, W. J. (2017). Superinsulating polyisocyanate based aerogels: A targeted search for the optimum solvent system. *ACS Applied Materials & Interfaces*, 9(21), 18222–18230. <https://doi.org/10.1021/acsami.7b03344>
- Zou, F., & Budtova, T. (2021). Polysaccharide-based aerogels for thermal insulation and superinsulation: An overview. *Carbohydrate Polymers*, 266, Article 118130. <https://doi.org/10.1016/j.carbpol.2021.118130>